DIRECT NUMERICAL SIMULATION OF TURBULENT FLOW THROUGH A SQUARE DUCT WITH LONGITUDINAL RIBS

Mark S. Tachie, Bing-Chen Wang
Department of Mechanical Engineering
University of Manitoba
Winnipeg, MB, R3T 5V6, Canada
tachiem@myumanitoba.ca, BingChen.Wang@umanitoba.ca

Wei-Jian Xiong
State Key Laboratory of Mechanics and Control of Aeronautics and Astronautics Structures
Nanjing University of Aeronautics and Astronautics
Nanjing, 29th Yudao Street, China
xwj@nuaa.edu.cn

ABSTRACT

Turbulent flows through a smooth- and a longitudinally-rib-roughened square duct are studied using direct numerical simulations (DNS) at Re_b = 2710 and 4400. The statistical moments of the turbulence field and dynamics of coherent structures are investigated in both physical and spectral spaces, which include analyses of the mean and instantaneous velocity fields, swirling strength and velocity spectra. Owing to the presence of the four sidewalls, secondary flow appears as four pairs of corner vortices in the smooth-duct and in the rib-roughened duct at the lower-Reynolds-number. By contrast, at the higher-Reynolds-number tested, it is interesting to observe additional tertiary vortices in the rib roughened duct, due to the increased heterogeneity of wall shear stresses. The effects of the ribs on the turbulent flow field are investigated by examining the profiles of shear stresses and budget balance of the turbulence kinetic energy (TKE), and by comparing the smooth- and ribbed-duct flows. It is observed that with the implementation of longitudinal ribs, hairpin structures become more densely populated while their size reduces as the Reynolds number increases. Through a spectral analysis, it is also observed that compared to the smooth-wall duct flow, the characteristic wavelength of the energetic streaky structures of the ribbed-duct flows shortens considerably.

INTRODUCTION

Turbulent flow within square ducts is ubiquitous in engineering with vast applications to, e.g. ventilation systems and heat exchangers. In contrast to a two-dimensional (2-D) boundary-layer flow developing over a flat plate, turbulent flow inside a duct is intrinsically three-dimensional (3-D), which features the interaction of boundary layers developing over the four sidewalls and formation of large secondary flow structures in the cross-stream plane. Furthermore, turbulent mixing can be intensified by introducing roughness elements in the form of transverse or longitudinal ribs. The presence of ribs profoundly alters the turbulence statistics and coherent flow structures, which further impact turbulent transport processes.

In the current literature, turbulent flow through a smooth square duct has been studied extensively both experimentally and numerically. Pirozzoli *et al.* (2018) studied the effects of Reynolds numbers on the secondary flows in a smooth square duct using DNS. Coletti *et al.* (2012) conducted detailed PIV experiments to investigate the effects of spanwise system rotation on turbulent flow in a transverse rib-roughened rectangular duct. Recently, Mahmoodi-Jezeh & Wang (2020) conducted DNS to compare three straight transverse rib duct flows of different blockage ratios against a smooth-duct flow, and concluded that secondary flows in a ribbed-duct generate a higher degree of non-equilibrium states in regions between the sidewall and duct center.

The current experimental and numerical studies of longitudinally-rib-roughened flows have mostly concentrated on 2-D boundary-layer flows developing over flat plates. Willingham *et al.* (2014) performed large-eddy simulations (LES) to study the impact of rib elements on turbulent mixing in a 2-D boundary layer. Vanderwall & Ganapathisubramani (2015) studied the effects of rib spacing on the development of secondary flows in a turbulent boundary layer. Notwithstanding the aforementioned contributions, studies on the combined effects of the vertical sidewalls and longitudinal ribs on a 3-D flow in a square duct are still lacking.

In view of this knowledge gap, the current research aims to study the turbulent flow through a duct roughened with square-shaped longitudinal ribs using DNS. The results of ribbed-duct flows are compared with those of a smooth-duct flow. The effects of Reynolds number on the flow within a ribbed-duct is explored by comparing the turbulence statistics at two Reynolds numbers.

TEST CASE AND NUMERICAL ALGORITHM

Figure 1 depicts the computational domain and coordinate system of the ribbed-duct flows. Here, the streamwise, vertical and spanwise coordinates are represented by x, y and z, and the corresponding velocity components are denoted as u, v and w, respectively. The streamwise domain length of the smooth- and ribbed-ducts is $L_x = 10\pi\delta$ and the vertical and spanwise widths are $L_y = L_z = 2\delta$. In the ribbed-ducts, square-shaped longitudinal ribs with side length $d/\delta = 2/7$ are placed at the center of each duct wall. The smooth-duct flow case is denoted as "SD", while the low and high Reynolds number ribbed-duct flow cases are denoted as "R1" and "R2", respectively. In cases SD and R2, the Reynolds number is maintained at $Re_b = D_h U_b/\nu = 4400$, while in case R1, $Re_b = 2710$. Here, D_h, U_b and ν represent the hydraulic diameter, bulk mean velocity and kinematic viscosity of the fluid, respec-
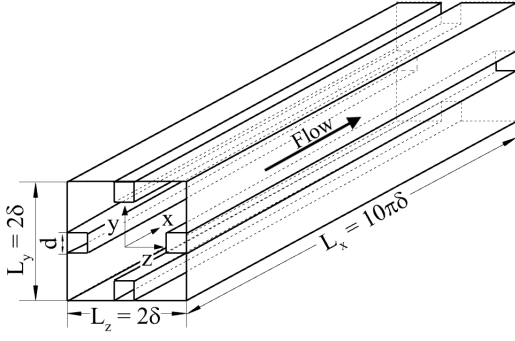
Figure 1: Computational domain and coordinate system of a square duct flow with square-shaped longitudinal ribs mounted on sidewalls.

Table 1: Geometry and flow parameters of the test cases.

Test case	Re_b	$U_b/U_{b,SD}$	Re_τ	d/δ	C_D
SD	4400	1	150	-	0.00929
R1	2710	0.88	127	2/7	0.00896
R2	4400	1.42	210	2/7	0.00929

tively. Specifically, the hydraulic diameters D_h are 2δ and $10/7\delta$ in the smooth-and ribbed-duct cases, respectively. The flow is fully developed and a periodic boundary condition is applied in the streamwise direction. A no-slip boundary condition is enforced at all solid walls. The governing equations for an incompressible flow are

$$\frac{\partial u_i}{\partial x_i} = 0 \quad , \tag{1}$$

$$\frac{\partial u_i}{\partial t} + u_j \frac{\partial u_i}{\partial x_j} = -\delta_{i1}\frac{\Pi}{\rho} - \frac{1}{\rho}\frac{\partial p}{\partial x_i} + \nu\frac{\partial^2 u_i}{\partial x_j \partial x_j} \quad , \tag{2}$$

where u_i, ρ and p denote the velocity, density and pressure of the fluid, respectively, and δ_{ij} is the Kronecker delta. A constant mean streamwise pressure gradient Π drives the flow.

The DNS was performed using a spectral-element code called "Semtex" (Blackburn & Sherwin, 2004). It is written in the C++ and FORTRAN programming languages, and utilizes message passing interface (MPI) libraries for parallelization. For the smooth- and ribbed-ducts, 1024 and 6864 quadrilateral finite elements were used in the cross-stream planes, respectively. Within each finite element, discretization was further achieved using a 4th-order Gauss-Lobatto-Legendre Lagrange polynomial. In both the smooth- and ribbed-ducts, all physical quantities are expanded into spectral space using Fourier expansion with 480 modes in the streamwise direction. The grid spacing in the streamwise direction is $\Delta x^+ = 9.82$, 8.29 and 13.72 for cases SD, R1 and R2, respectively, and varies as $\Delta y^+ = \Delta z^+ = 0.12$-4.80, 0.06-4.20 and 0.10-6.95 in the spanwise and vertical directions for cases SD, R1 and R2, respectively. The wall units (i.e., $\Delta n^+ = nu_{\tau,a}/\nu$) are defined based on the time- and surface-averaged wall friction velocity $u_{\tau,a} = \sqrt{\langle \oint_P (\tau_w/\rho)\mathrm{d}l/P\rangle}$, where the integration is done over the perimeter P of a cross section while $\tau_w = \rho\nu(\partial\langle u\rangle/\partial n)_{wall}$ is the local wall viscous stress and $\langle\cdot\rangle$ represents averaging over time and over the homogeneous (x) direction. As such, the value of $u_{\tau,a}$ is a function of the pressure gradient only, i.e. $u_{\tau,a} = f(\Pi)$. Overall, the Semtex code is highly accurate for conducting DNS, as the resolution is of a spectral accuracy. In the smooth- and ribbed-duct flows, 1200 and 400 instantaneous flow fields were generated, respectively, to compute flow statistics subsequent to precursor simulations once the flows became statistically stationary. All simulations were performed on the Grex supercomputers of the University of Manitoba.

RESULTS AND DISCUSSION

Table 1 summarizes the key flow parameters of the smooth-wall and ribbed-duct flow cases. Here, the friction

Reynolds number ($Re_\tau = \delta u_{\tau,a}/\nu$) is based on the time- and surface-averaged wall friction velocity $u_{\tau,a}$ and the drag coefficient is defined as follows:

$$C_D = \frac{F_D}{0.5\rho U_b^2 A_w} \quad , \tag{3}$$

where F_D (defined as $F_D = \int_{A_w} \tau_w dA_w$) and A_w are the friction drag and wetted area, respectively. It is noted that due to the implementation of the ribs, the wetted area in the ribbed-duct flows is 9/7 times that of the smooth-wall duct flow. Comparing cases SD and R2, it is evident that longitudinal ribs do not alter the value of the drag coefficient. Results for the ribbed-duct flow cases demonstrate the value of C_D increases by 3.68% as the Reynolds number increases from $Re_b = 2710$ to 4400.

Figure 2 compares contour plots of the non-dimensionalized instantaneous cross-stream velocity u_{cs}/U_b (left-panel) and streamwise velocity u/U_b (right-panel) of cases SD, R1 and R2. From the right-panels of Figs. 2(a), (b) and (c), it is apparent that "mushroom patterns" are present in each flow case. By comparing with the SD case, in the two ribbed cases R1 and R2, the strength of vortices tends to be the largest adjacent to the rib edges. Further by comparing Figs. 2(b) and (c), it is apparent that instantaneous secondary flow structures are stronger and more populous throughout the ribbed flow domain at the higher-Reynolds-number tested.

Figure 3 presents the non-dimensionalized mean streamwise velocity contours $\langle u\rangle/U_b$ superimposed with streamlines of the mean cross-stream velocity vector ($\langle v\rangle$ and $\langle w\rangle$) of all three test cases in the cross-stream plane. Due to the symmetry of the mean flow field, only half of the domain of case R2, and a quarter of the domains of cases SD and R1 are plotted in Fig. 3 to enable a direct comparison. By comparing cases R1 and SD, it is clear the flow field of R2 shows more vertical and spanwise heterogeneity. The Reynolds number effects are apparent by comparing cases R1 and R2. Unlike cases SD and R1 which only exhibit secondary flows, case R2 exhibits tertiary flows indicating that the near-wall flow physics have been significantly altered.

Figure 4 compares the profiles of the skin friction coefficient ($C_f = \tau_w/(\rho U_b^2/2)$) along the bottom wall of the smooth- and ribbed-duct flow cases. In the smooth-duct flow, the skin friction coefficient is 0 at a duct corner and rapidly increases to $C_f \approx 0.01$ as the sidewall center is approached. The skin friction coefficient in the ribbed-duct flows exhibits a complex and interesting pattern, which is also 0 at the duct corner, rapidly increases to $C_f \approx 0.01$, but decays again to 0 as the intersection of the rib and the horizontal sidewall is approached. Thereafter, C_f increases and a sharp peak is observed at the rib edges of cases R1 and R2, which is contributed primarily by wall shear stress component τ_{13} such that the neighbourhood of rib edges features stress concentration. Furthermore, the magnitude of this sharp peak decreases from $C_f \approx 0.085$ to 0.06 as the Reynolds number increases from $Re_b = 2710$ to 4400.

(a) Case SD
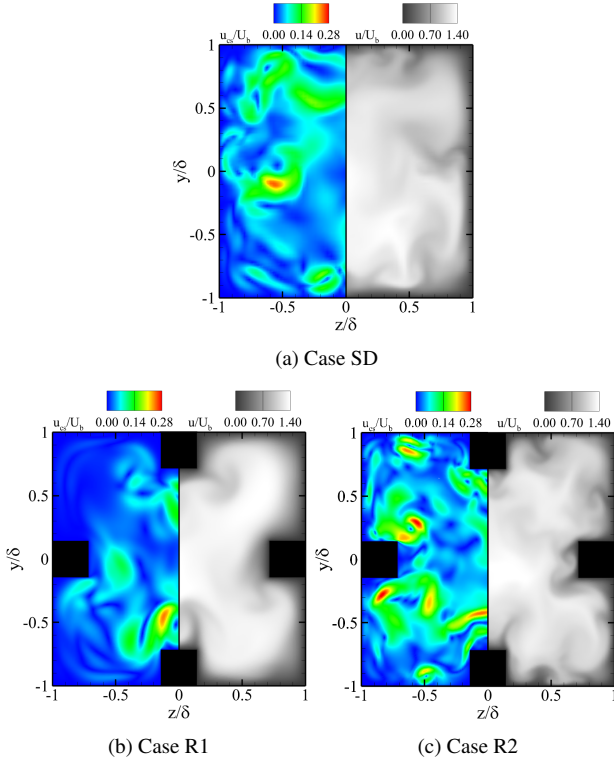

(b) Case R1

(c) Case R2

Figure 2: Cross-stream distribution of the non-dimensionalized instantaneous cross-stream velocity u_{cs}/U_b (left-panel) and instantaneous streamwise velocity u/U_b (right-panel) of cases SD, R1 and R2, respectively. Each contour pattern is mapped at the same flow through time ($t = 200$) and at the same streamwise location ($x/\delta = 5\pi$).
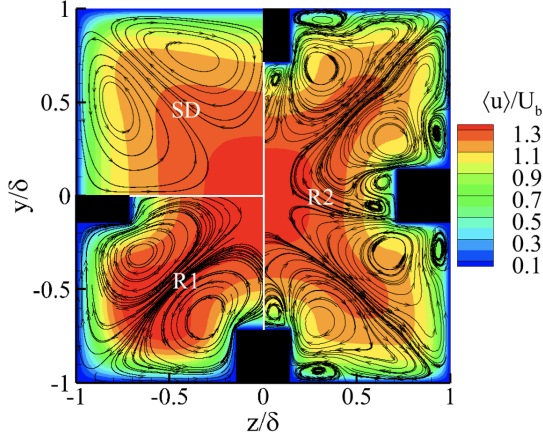

Figure 3: Mean streamwise velocity $\langle u \rangle /U_b$ superimposed with streamlines of the mean cross-stream velocity vector ($\langle v \rangle$ and $\langle w \rangle$) for the three test cases of SD, R1 and R2.

Figure 5 presents vertical profiles of the non-dimensionalized mean streamwise velocity $\langle u \rangle /U_b$ for cases SD, R1 and R2. The profiles are analyzed at $z/\delta = 0.0$, 0.5 and 0.7 to quantitatively assess the effects of longitudinal ribs and Reynolds number on the mean flow field. In the central vertical plane ($z/\delta = 0.0$), the profiles of all three test cases are qualitatively similar. Specifically, in the smooth-wall and ribbed-duct flow cases, $\langle u \rangle /U_b$ monotonically approaches a single maxima at the duct center. However, because of the influence of the ribs, the profiles along the vertical lines
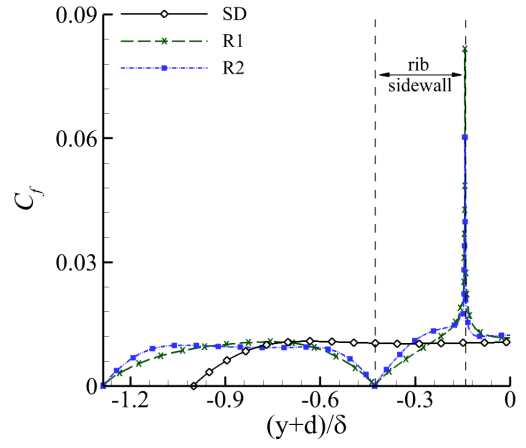

Figure 4: Profiles of the skin friction coefficient $C_f = \tau_w/(\rho U_b^2/2)$ along the bottom wall for cases SD, R1 and R2.
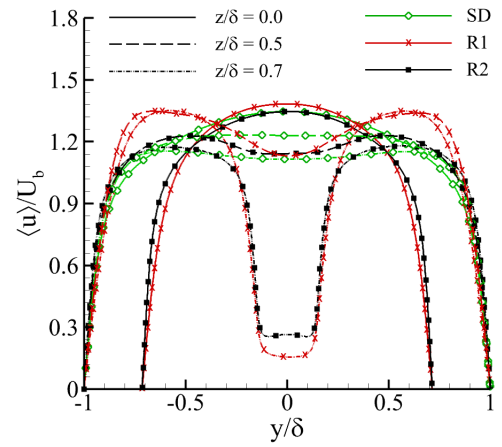

Figure 5: Vertical profiles of the non-dimensionalized mean streamwise velocity $\langle u \rangle /U_b$ examined at $z/\delta = 0.0$, 0.5 and 0.7 for cases SD, R1 and R2, respectively.

$z/\delta = 0.5$ and 0.7 are notably different at the duct core as they exhibit flat and saddle-back shapes, respectively. In the central vertical plane ($z/\delta = 0.0$), the Reynolds number effect is evident as the center line velocity of the low-Reynolds-number case R1 is higher than that of the higher-Reynolds-number case R2.

Figure 6 compares vertical profiles of the non-dimensionalized Reynolds normal stresses ($\langle u'u' \rangle /U_b^2$, $\langle v'v' \rangle /U_b^2$ and $\langle w'w' \rangle /U_b^2$) of cases SD, R1 and R2. From Fig. 6(a), it is seen that although the wall conditions differ, the profiles of the Reynolds normal stresses of both smooth- and ribbed-duct flows are qualitatively similar at this central vertical position ($z/\delta = 0.0$). Clearly, the streamwise Reynolds normal stress $\langle u'u' \rangle /U_b^2$ has the highest magnitude, followed by the spanwise and vertical Reynolds normal stresses (i.e., $\langle w'w' \rangle /U_b^2$ and $\langle v'v' \rangle /U_b^2$, respectively). Upon further inspection, the magnitude of $\langle u'u' \rangle /U_b^2$ is the greatest in the smooth-wall duct flow, while $\langle w'w' \rangle /U_b^2$ and $\langle v'v' \rangle /U_b^2$ have the highest magnitudes in the high-Reynolds-number ribbed-duct flow case. Comparing the ribbed-duct flow cases, a higher magnitude of the streamwise Reynolds normal stress $\langle u'u' \rangle /U_b^2$ is exhibited in case R1.

Figure 6(b) compares the vertical profiles of the Reynolds normal stresses of three test cases at an off-center position near the rib edge ($z/\delta = 0.7$). The rib effects on the Reynolds nor-
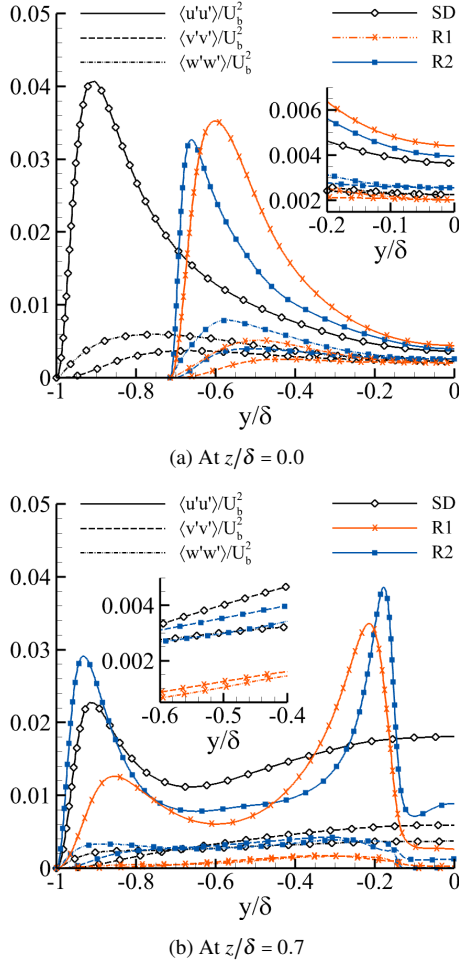
(a) At $z/\delta = 0.0$

(b) At $z/\delta = 0.7$

Figure 6: Vertical profiles of the non-dimensionalized Reynolds normal stresses ($\langle u'u'\rangle/U_b^2$, $\langle v'v'\rangle/U_b^2$ and $\langle w'w'\rangle/U_b^2$) examined at $z/\delta = 0.0$ and 0.7 for cases SD, R1 and R2, respectively.

mal stresses are clear by comparing ribbed-duct cases R1 and R2 against the smooth-duct case SD. In case SD, the streamwise Reynolds normal stress $\langle u'u'\rangle/U_b^2$ attains a maximum in the near-wall region, and decays to a local minimum before approaching a local maximum at the duct center. By contrast, in the ribbed-duct cases R1 and R2, the profile of $\langle u'u'\rangle/U_b^2$ reaches a local maximum in the near-wall region, and subsequently decays to a local minimum before attaining its highest magnitude near the rib edges. In the ribbed-duct flows, the profiles of the vertical and spanwise Reynolds normal stresses are more complex compared to those of a smooth-wall duct flow. Specifically, at the duct center of the ribbed-duct flow cases, the values of $\langle v'v'\rangle/U_b^2$ and $\langle w'w'\rangle/U_b^2$ are much lower than that of the smooth-duct flow, which is attributed to the vertical sidewall effects. Clearly, in the ribbed-duct flows, the mixing properties are the greatest near rib edges as opposed to smooth-wall duct flows whose mixing are the greatest at the duct wall center. The Reynolds number effects on the ribbed-duct flow are evident by comparing the profiles of cases R1 and R2. Clearly, the magnitudes (especially the peak magnitudes) of all three Reynolds normal stresses become larger as the Reynolds number increases from $Re_b = 2710$ to 4400.

Figure 7 compares vertical profiles of the non-dimensionalized viscous, Reynolds and total shear stress of τ_{12} (i.e. τ_{12}^{vis+}, τ_{12}^{turb+} and τ_{12}^{tot+}, respectively) in the smooth- and ribbed-duct flow cases. These three shear stresses bal-

ance as $\tau_{12}^{tot+} = \tau_{12}^{vis+} + \tau_{12}^{turb+}$. The profiles are examined in the central vertical (at $z/\delta = 0.0$) plane and near the rib edge (at $z/\delta = 0.7$). Figure 7(a) illustrates that along the central vertical line $z/\delta = 0.0$, the vertical profiles of τ_{12}^{vis+}, τ_{12}^{turb+} and τ_{12}^{tot+} are qualitatively similar among the three test cases, despite that their boundary positions and Reynolds numbers differ. Precisely, the viscous shear stress dominates the near-wall region while the Reynolds stress dominates the central core of the duct. Furthermore, different from the classical plane-channel flow (Kim & Moin, 1987), the total shear stress τ_{12}^{tot+} deviates from a strict linear distribution.

Figure 7(b) presents the vertical profiles of τ_{12}^{vis+}, τ_{12}^{turb+} and τ_{12}^{tot+} at an off-center position near the rib edge ($z/\delta = 0.7$) for all three test cases. In the smooth-duct flow, the maximum shear stress occurs at the duct walls (in a central vertical plane). However, the total shear stress diminishes more rapidly at $z/\delta = 0.7$ than at $z/\delta = 0.0$. It is also observed that in comparison to the profiles in the central vertical plane, the magnitude of the Reynolds shear stress τ_{12}^{turb+} is lower in the off-center plane at $z/\delta = 0.7$, and its sign switches from positive to negative within one half of the duct. Clearly, in comparison with test cases SD and R1, the peak magnitude of the Reynolds stress is much higher in the higher-Reynolds-number case R2 in regions near the duct center. Furthermore, it is observed that unlike the higher-Reynolds-number tested, the magnitude of the viscous and Reynolds shear stresses are comparable near the rib edges. This may explain the higher peak value of C_f of case R1 than that of case R2 as depicted in Fig. 4.

To refine the study of rib effects on the turbulent transport process, the budget balance of the turbulence kinetic energy (TKE), defined as $k = 0.5(\langle u'u'\rangle + \langle v'v'\rangle + \langle w'w'\rangle)$, of the smooth- and ribbed-duct flows can be investigated. Under the steady flow condition, the transport equation of TKE is expressed as:

$$H_k = P_k + D_k^t + D_k^p + D_k^v - \varepsilon_k \quad , \qquad (4)$$

where H_k, P_k, D_k^t, D_k^p, D_k^v and ε_k denote the convection, turbulent production, turbulent diffusion, pressure diffusion, viscous diffusion and dissipation terms, respectively. These terms are expressed, respectively, as follows:

$$H_k = \langle u_j\rangle \frac{\partial k}{\partial x_j} \quad , \qquad (5)$$

$$P_k = -\langle u_i'u_j'\rangle \frac{\partial \langle u_i\rangle}{\partial x_j} \quad , \qquad (6)$$

$$D_k^t = -\frac{1}{2}\frac{\partial \langle u_i'u_i'u_j'\rangle}{\partial x_j} \quad , \qquad (7)$$

$$D_k^p = -\frac{1}{\rho}\frac{\partial \langle p'u_j'\rangle}{\partial x_j} \quad , \qquad (8)$$

$$D_k^v = v\frac{\partial^2 k}{\partial x_j^2} \quad , \qquad (9)$$

$$\varepsilon_k = v\left\langle \frac{\partial u_i'}{\partial x_j}\frac{\partial u_i'}{\partial x_j}\right\rangle \quad . \qquad (10)$$

Figure 8 shows the budget balance of TKE along the central vertical line (at $z/\delta = 0$) and at an off-center position near the rib edge ($z/\delta = 0.7$). From Figs. 8(a), (c) and (d), it is seen that the profiles of the budget terms of the smooth- and ribbed-duct flow cases behave qualitatively similar despite that their vertical boundary positions are different. Namely, at the walls, the viscous diffusion (D_k^v) and dissipation (ε_k) terms are the lead source and sink terms, respectively. In the near-wall region, the production term (P_k) peaks as a source of TKE whereas the turbulent diffusion and dissipation terms (D_k^t and ε_k) act as
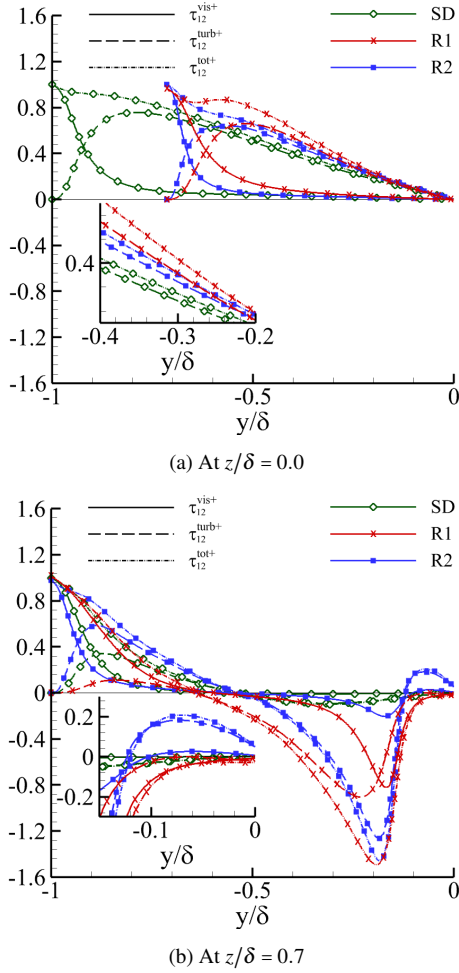
(a) At $z/\delta = 0.0$

(b) At $z/\delta = 0.7$

Figure 7: Vertical profiles of non-dimensionalized viscous, Reynolds and total shear stresses (i.e. τ_{12}^{vis+}, τ_{12}^{turb+} and τ_{12}^{tot+}, respectively) evaluated at $z/\delta = 0.0$ and 0.7 for the smooth-wall and ribbed-duct flow cases, respectively.

(a) Case SD at $z/\delta = 0.0$ — (b) Case SD at $z/\delta = 0.7$

(c) Case R1 at $z/\delta = 0.0$ — (d) Case R1 at $z/\delta = 0.7$

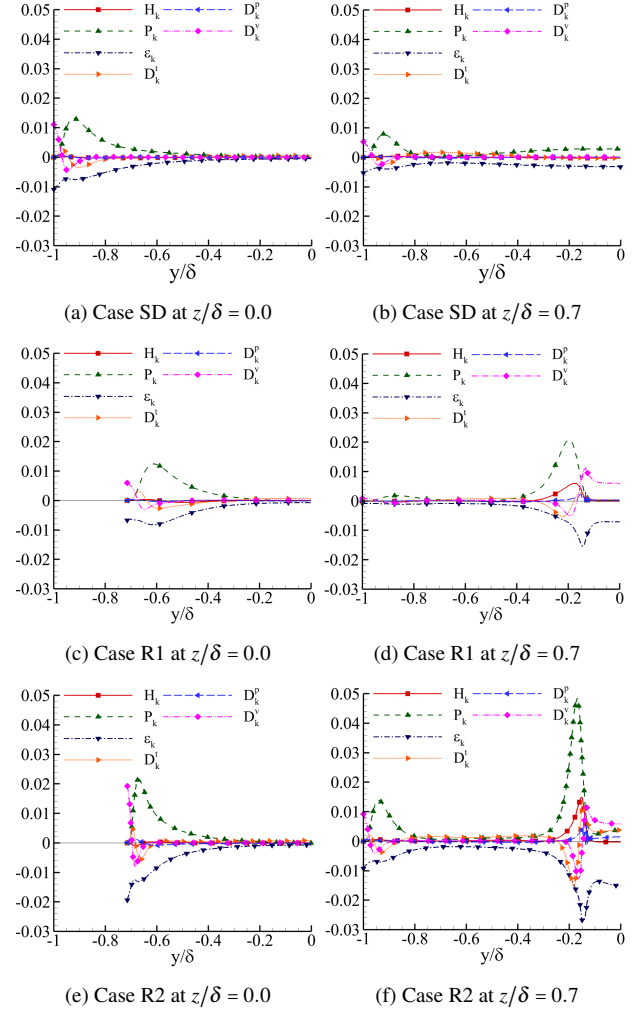(e) Case R2 at $z/\delta = 0.0$ — (f) Case R2 at $z/\delta = 0.7$

Figure 8: Vertical profiles of the budget terms of TKE evaluated at $z/\delta = 0.0$ and 0.7 for cases SD, R1 and R2. All budget terms have been non-dimensionalized by U_b^3/δ.

sinks. As the duct center is approached, each term approaches a local minimum and it is noted the convection term is trivial at $z/\delta = 0.0$. By comparing the SD, R1 and R2 cases, it is conspicuous that aside from the convection term, the magnitudes of all budget terms are greater in the higher-Reynolds-number ribbed-duct flow case.

Figures 8(b), (d) and (f) show profiles of the budget terms of TKE at an off-center position near the rib edge ($z/\delta = 0.7$). The impact of the ribs on the budget balance of the TKE is evident by comparing Figs. 8(a), (c) and (e) with Figs. 8(b), (d) and (f), especially in regions for $y/\delta \geq -0.35$. In the smooth-duct flow case, all budget term peak in the near wall region. By contrast, the budget terms have the primary peaks near the ribs in cases R1 and R2. It is also worth mentioning that unlike the smooth-wall duct flow, the convection term is non-trivial and contributes to the TKE energy balance in the ribbed-duct flows. Near the rib edges, the production and pressure diffusion terms act as energy sources, the convection and dissipation terms as sinks, whereas the turbulent and viscous diffusion terms act as both sources and sinks. Clearly, the rib effect is to enhance the magnitude of the production term, and the contribution of H_k in the energy balance is attributed to the increased turbulence non-equilibrium ($P_k \neq \varepsilon_k$) in the two ribbed-duct flow cases R1 and R2. The magnitudes of the budget terms are noticeably greater in the higher-Reynolds-number case R2

than in the lower-Reynolds-number case R1, further highlighting the Reynolds number effect on ribbed-duct flows.

Figure 9 displays isopleths of the non-dimensional 1-D pre-multiplied energy spectra $\delta k_x \phi_{uu}/U_b^2$ in the y-λ_x plane at $z/\delta = 0$ of the three test cases. Here, k_x denotes the streamwise wavenumber, λ_x represents the streamwise wavelength, and all quantities have been non-dimensionalized by U_b and δ. The characteristic streamwise wavelength of the most energetic streaky structures is the longest in case SD, in comparison with those of the two ribbed-duct flow cases R1 and R2. Clearly, as one of the rib effects, the vertical position y/δ (indicated by a star symbol in Fig. 9) of the most energetic streaky structures has significantly elevated in the two ribbed-duct cases R1 and R2. It is noted that $\delta k_x \phi_{uu}/U_b^2$ has a higher magnitude in the lower-Reynolds-number tested.

Figures 10(a), (b) and (c) contrast the instantaneous vortical structures (visualized using the λ_{ci}-criterion and coloured by the non-dimensionalized instantaneous streamwise velocity u/U_b). For clarity, only half the streamwise domain length (for $x/\delta \in [0, 5\pi\delta]$) is illustrated. To facilitate a fair comparison, the non-dimensionalized swirling strength is kept constant, with $\lambda_{ci}\delta/U_b = 2.1$ in all three test cases. From Fig. 10(a), it is clear that the flow structures are sparse in the smooth-wall duct flow. Figure 10(b) illustrates that the vortical structures are sparse, but concentrated near the rib edges. By contrast,
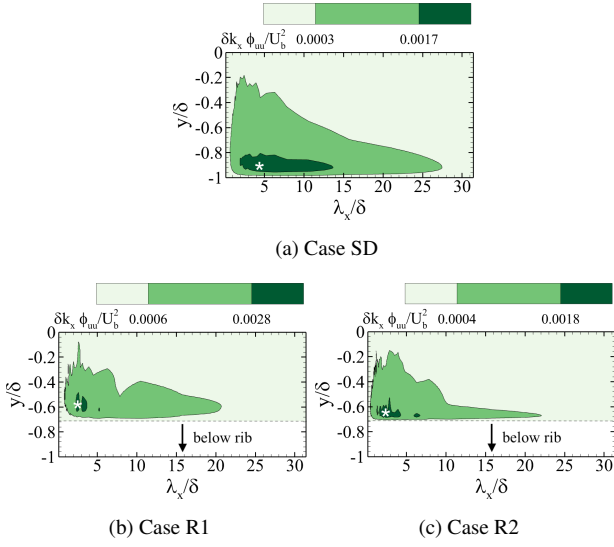
(a) Case SD

(b) Case R1

(c) Case R2

Figure 9: Isopleths of the streamwise 1-D pre-multiplied energy spectra $k_x\phi_{uu}$ non-dimensionalized by U_b^2/δ in the central vertical plane (located at $z/\delta = 0$) of the three test cases. The star symbol "$\ast$" denotes the peak location. The inner and outermost isopleths correspond to high and low turbulence energy levels of $k_x\phi_{uu} = 0.625\max(k_x\phi_{uu})$ and $0.125\max(k_x\phi_{uu})$, respectively.

Fig. 10(c) shows that as the Reynolds numbed increases, the flow structures become more abundant throughout the duct domain, especially near the rib edges.

CONCLUSIONS

Internal turbulent flows through smooth-wall and longitudinally-rib-roughened square duct flows have been investigated using DNS. In order to examine the rib effects and Reynolds number effects on the flow physics, the smooth- and ribbed-duct flows are compared at $Re_b = 4400$, while an additional ribbed-duct flow case is simulated at a lower-Reynolds-number of $Re_b = 2710$. With the implementation of longitudinal ribs, it was observed that large instantaneous low momentum flows structures move from the duct walls (as in a smooth-duct flow) towards the rib edges of a ribbed-duct flow. Additional to the secondary mean flow structures shown in cases SD and R1, it is interesting to observe tertiary flow vortices in the higher-Reynolds-number ribbed-duct flow case R2.

The study illustrated that in the central vertical plane, the profiles of the smooth- and ribbed-duct flows are qualitatively similar, but in the off-center vertical planes, the profiles of the ribbed-duct flows become more complex, especially near the vertical sidewall. Through an examination of the Reynolds normal stresses and the total shear stress profiles, it was discovered that the anisotropy of the Reynolds stress tensor is enhanced by the presence of longitudinal ribs. Based on a study of the transport process of TKE, it is observed that each budget term reaches its maximum magnitude near the rib edge in a ribbed-duct flow, and furthermore, has a higher magnitude in the higher-Reynolds-number case tested. It is observed that with the implementation of longitudinal ribs, vortical structures are concentrated near the rib edges. In fact, the characteristic streamwise wavelength of the most energetic streaky structures is the longest in the smooth-duct case SD in comparison with those of the two ribbed-duct flow cases R1 and R2.
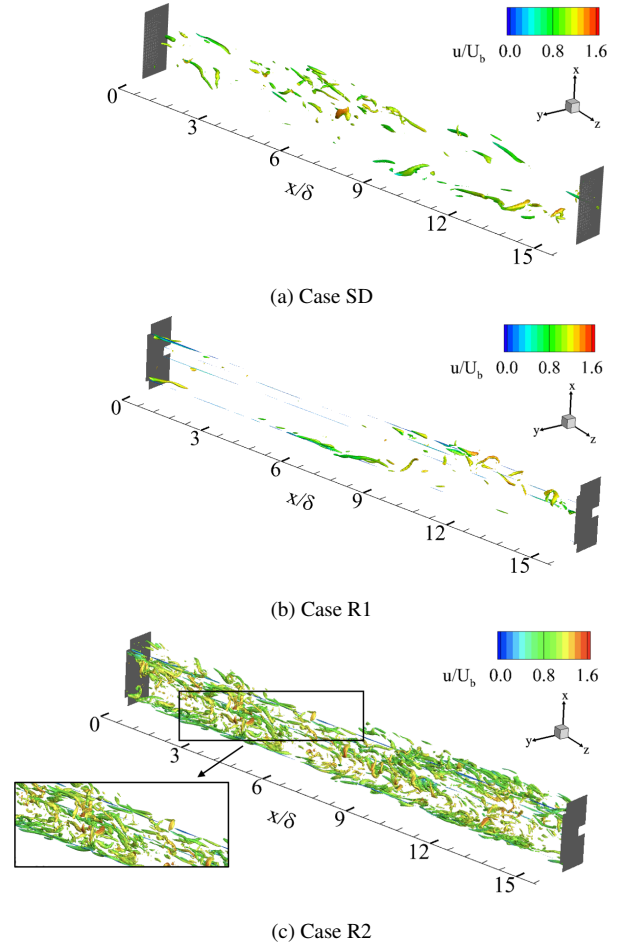

(a) Case SD

(b) Case R1

(c) Case R2

Figure 10: Contours of coherent structures visualized using the λ_{ci} criterion (for $\lambda_{ci}\delta/U_b = 2.1$), coloured by the instantaneous non-dimensionalized streamwise velocity (u/U_b) within the streamwise domain of $x/\delta \in [0, 5\pi\delta]$ for cases SD, R1 and R2.

REFERENCES

Colleti, F., Maurer, T., Art, T. & Di Sante, A. 2012 Flow field investigation in rotating rib-roughened channel by means of particle image velocimetry. *Exp. Fluids* **52**, 1043–1061.

Blackburn, H. M. & Sherwin, S. J. 2004 Formulation of a Galerkin spectral element–Fourier method for three-dimensional incompressible flows in cylindrical geometries. *J. Comp. Phys.* **197** (2), 759–778.

Mahmoodi-Jezeh, S. V. & Wang, B.-C. 2020 Direct numerical simulation of turbulent flow through a ribbed square duct. *J. Fluid Mech.* **900**, 1–43.

Pirozzoli, S., Modesti, D., Orlandi, P. & Grasso, F. 2018 Turbulence and secondary motions in square duct flow. *J. Fluid Mech.* **840**, 631–655.

Vanderwel, C. & Ganapathisubramani, G. 2015 Effects of spanwise spacing on large-scale secondary flows in rough-wall turbulent boundary layers. *J. Fluid Mech.* **774**, R2.

Willingham, D., Anderson, W., Christensen, K. T. & Barros, J. M. 2014 Turbulent boundary layer flow over transverse aerodynamic roughness transitions: induced mixing and flow characterization. *Phys. Fluids* **26** (2), 025111.

Kim, J., Moin, P. & Moser, R. 1987 Turbulent statistics in fully developed channel flow at low Reynolds number. *J. Fluid Mech.* **177**, 133–166.